

ARTICLE

Open Access

Strategies to approach high performance in Cr³⁺-doped phosphors for high-power NIR-LED light sources

Zhenwei Jia^{1,2}, Chenxu Yuan^{1,3}, Yongfu Liu¹, Xiao-Jun Wang⁴, Peng Sun¹, Lei Wang², Haochuan Jiang¹ and Jun Jiang¹

Abstract

Broadband near-infrared (NIR)-emitting phosphors are key for next-generation smart NIR light sources based on blue LEDs. To achieve excellent NIR phosphors, we propose a strategy of enhancing the crystallinity, modifying the micromorphology, and maintaining the valence state of Cr³⁺ in Ca₃Sc₂Si₃O₁₂ garnet (CSSG). By adding fluxes and sintering in a reducing atmosphere, the internal quantum efficiency (IQE) is greatly enhanced to 92.3%. The optimized CSSG:6%Cr³⁺ exhibits excellent thermal stability. At 150 °C, 97.4% of the NIR emission at room temperature can be maintained. The fabricated NIR-LED device emits a high optical power of 109.9 mW at 520 mA. The performances of both the achieved phosphor and the NIR-LED are almost the best results until now. The mechanism for the optimization is investigated. An application of the NIR-LED light source is demonstrated.

Introduction

NIR spectroscopy has good penetration for organic matter, and it has drawn attention for application in monitoring foods and medicines, bioimaging, and night vision^{1–6}. Smart NIR light sources, an emerging field, are proposed to be combined with smart phones to achieve convenient and fast applications^{7–9}. In contrast to traditional tungsten filament lamps and halogen lamps, only light-emitting diodes (LEDs) that have a solid state and a small size are suitable for smart NIR devices. However, NIR-LED chips can only give narrow NIR emissions, which limits their applications^{10–12}. Broad NIR-emitting phosphor-converted (pc) LEDs, adopting the technology of pc-white LEDs^{13–19}, are believed to be the best solution. White LEDs are commonly based on blue-LED

chips. Thus, how to achieve broad NIR phosphors that can be efficiently excited by blue light is one of the most important challenges²⁰.

Recently, a number of NIR phosphors were realized^{21–44}. Among them, Cr³⁺ usually manifests a high efficiency, and the IQE can reach 58–75%^{31–37}. The radiant power is 14.7–54.29 mW when driven at 100–130 mA^{34–40}. A high radiant power is beneficial for monitoring and detection. Liu et al made great progress in improving the radiant power, which was enhanced from 7–18.2 mW^{42,43} to 65.2 mW⁴⁴ when driven at 350 mA. To achieve high radiance, a high-power LED chip operating at a high current is usually needed. In this situation, the large amount of heat will result in a high temperature on the surface of the chip. Thus, the greatest challenge is how to make NIR phosphors have excellent thermal stability to overcome the thermal quenching effect, in addition to a high QE for NIR phosphors.

We note that Cr³⁺ has a high QE in garnets^{34,35}. The silicate garnet Ca₃Sc₂Si₃O₁₂ (CSSG) is a promising host for Cr³⁺ due to its excellent thermal stability and high QE^{45–47}. Fortunately, Cr³⁺ can be excited by blue light and show

Correspondence: Yongfu Liu (liuyongfu@nimte.ac.cn) or Lei Wang (wanglei_keke@163.com)

¹Ningbo Institute of Materials Technology & Engineering, Chinese Academy of Sciences, Ningbo 315201, China

²College of Physics and Optoelectronics, Taiyuan University of Technology, Taiyuan 030024, China

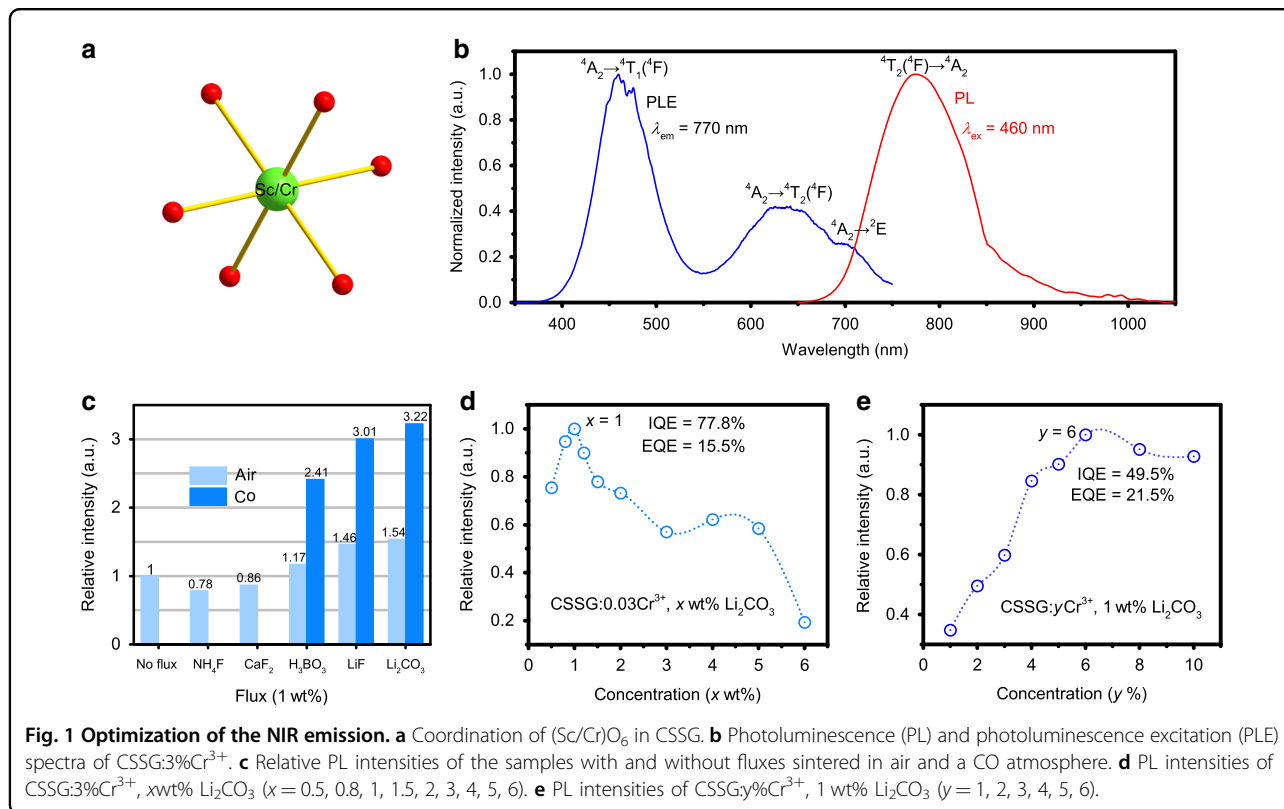
Full list of author information is available at the end of the article

These authors contributed equally: Zhenwei Jia, Chenxu Yuan

© The Author(s) 2020



Open Access This article is licensed under a Creative Commons Attribution 4.0 International License, which permits use, sharing, adaptation, distribution and reproduction in any medium or format, as long as you give appropriate credit to the original author(s) and the source, provide a link to the Creative Commons license, and indicate if changes were made. The images or other third party material in this article are included in the article's Creative Commons license, unless indicated otherwise in a credit line to the material. If material is not included in the article's Creative Commons license and your intended use is not permitted by statutory regulation or exceeds the permitted use, you will need to obtain permission directly from the copyright holder. To view a copy of this license, visit <http://creativecommons.org/licenses/by/4.0/>.



broadband NIR emission in CSSG³⁹. Unfortunately, the reported luminescence (IQE: 12.8%) and thermal stability were low because the Cr $^{3+}$ luminescence suffered from impurities and oxidation of Cr $^{4+}$ when the material was sintered in air³⁹. Based on our previous experience, we propose a strategy to optimize CSSG:Cr $^{3+}$ by enhancing the crystallinity, modifying the micromorphology, and maintaining the valence state of Cr $^{3+}$. By adding fluxes and sintering in a CO reducing atmosphere, the IQE is greatly enhanced to 92.3%. At 150 °C, 97.4% of the NIR emission at room temperature can be maintained, indicating excellent thermal stability. When combined with a high-power 460 nm blue chip, the estimated radiant power of the fabricated pc-LED even reaches 109.9 mW when driven at 520 mA. The properties of both the optimized CSSG:Cr $^{3+}$ and the achieved NIR-LED are almost the best results to date as far as we know. Benefiting from the high radiant power, the pc-NIR-LED device has good application potential in night-vision technology.

In this work, mechanisms for optimization were investigated. The electron–phonon coupling (EPC) mechanism in CSSG that usually determines the Cr $^{3+}$ luminescence is revealed for the first time. Many types of Cr $^{3+}$ -doped NIR phosphors have been discovered. We believe that this work provides an effective strategy to optimize and discover more Cr $^{3+}$ -doped NIR phosphors using only a simple method. Moreover, this work will advance the

development and application of next-generation smart NIR light sources.

Results

Optimization of CSSG:Cr $^{3+}$

CSSG belongs to a cubic crystal system with the space group of $I\alpha 3d$ (Fig. S1). Ca, Sc, and Si are coordinated with 8, 6, and 4 oxygen atoms, respectively^{45–47}. Considering the effective ionic radii of Ca $^{2+}$ (1.12 Å), Sc $^{3+}$ (0.745 Å), Si $^{4+}$ (0.26 Å), and Cr $^{3+}$ ($r = 0.615$ Å), it is believed that Cr $^{3+}$ occupies the Sc $^{3+}$ site due to the close radii and same ionic valence³⁹. Thus, Cr $^{3+}$ suffers from a weak crystal field (CF) environment in the ScO $_6$ octahedron (Fig. 1a). The spin-allowed transitions of $^4A_{2g} \rightarrow ^4T_{1g}(^4F)$ and $^4A_{2g} \rightarrow ^4T_{2g}(^4F)$ lead to two excitation bands centered at 460 and 640 nm, respectively (Fig. 1b). The spin-forbidden transition of $^4A_{2g} \rightarrow ^2E_g(^2G)$ (R-line) at ~ 701 nm is also detected. Under 460 nm excitation, CSSG:Cr $^{3+}$ shows a broad NIR emission peaking at ~ 770 nm with a full-width at half maximum (FWHM) value of ~ 1750 cm $^{-1}$ (~ 110 nm), arising from the $^4T_{2g}(^4F)$ to $^4A_{2g}$ transition of Cr $^{3+}$ in the weak CF.

CSSG:Cr $^{3+}$ synthesized in an air atmosphere exhibits a weak NIR emission (Figs. S2–5), which could be attributed to a lower crystallinity and oxidation of Cr $^{3+}$ ³⁹. For the optimized Cr $^{3+}$ concentration, that is, CSSG:3%Cr $^{3+}$, its IQE and external quantum efficiency (EQE) are quite

low, only ~12.8% and 4.8%, respectively (Fig. S6). To enhance the luminescence by improving the crystallinity, fluxes of NH_4F , CaF_2 , H_3BO_3 , LiF , and Li_2CO_3 were added during the synthesis under the air condition. The NIR emission of the flux-free sample was set as the normalized standard. As Fig. 1c shows, H_3BO_3 , LiF , and Li_2CO_3 enhance the luminescence, while NH_4F and CaF_2 decrease the luminescence. Thus, H_3BO_3 , LiF , and Li_2CO_3 were selected, and CSSG:3% Cr^{3+} was sintered in a CO reducing atmosphere to further maintain the state of Cr^{3+} . It is noted that the luminescence is greatly enhanced by 2~3 times. Li_2CO_3 has the best effect, and the optimal amount is 1 wt% (Fig. 1d). Correspondingly, the IQE and EQE of CSSG:3% Cr^{3+} reach ~77.8% and 15.5%, respectively. Moreover, by adding 1 wt% Li_2CO_3 and sintering in CO, the Cr^{3+} concentration is optimized to 6% (Fig. 1e). Then, the achieved EQE of CSSG:6% Cr^{3+} even reaches 21.5%. Here, the QE is the measured result. Due to the limitation of the measurement, up to 850 nm, the results are smaller than the actual values, which will be illustrated later. Therefore, the actual QE is almost the best value among NIR phosphors as far as we know.

Crystal structures and micromorphology

To clarify the enhancement of the optimized CSSG: Cr^{3+} compared with the initial phosphor, the crystal structures and micromorphology were studied. For CSSG:3% Cr^{3+} sintered in air (Fig. 2a), the X-ray diffraction (XRD) pattern mainly shows a garnet phase of CSSG (PDF # 72-1969), but a few impurity phases of SiO_2 and Sc_2O_3 are also observed. These impurity phases can also be observed in the SEM-EDS mapping images. Ca, Sc, Si, O, and Cr are inhomogeneously distributed in the square region, in which Sc is rich and Si and Ca are absent.

For CSSG:3% Cr^{3+} sintered in CO with 1 wt% Li_2CO_3 (Fig. 2b), the SiO_2 and Sc_2O_3 impurities are quite low in the XRD pattern. The distributions of elements are more homogeneous. In addition, the diffraction peak intensity of the CSSG phase increases (Fig. 2c). These results demonstrate that the enhanced crystallinity of the CSSG phase is one of the reasons for the improvement of the Cr^{3+} NIR emissions.

The CSSG:3% Cr^{3+} phosphor has a particle size of ~10 μm (Fig. 2d). The particle displays a small variation in the cathodoluminescence (CL), as the CL image shows. The bright region (point I) and the dark region (point II) are only different in CL intensity. Their normalized CL spectra are almost the same, having an emission peak at ~760 nm and an FWHM of 1583–1590 cm^{-1} (93–94 nm), similar to the photoluminescence (PL) spectrum in Figs. S2–S5.

Diagnosis of the valence state of Cr^{3+}

To diagnose the change in the ionic valence of Cr, X-ray photoelectron spectroscopy (XPS), diffuse reflection (DR),

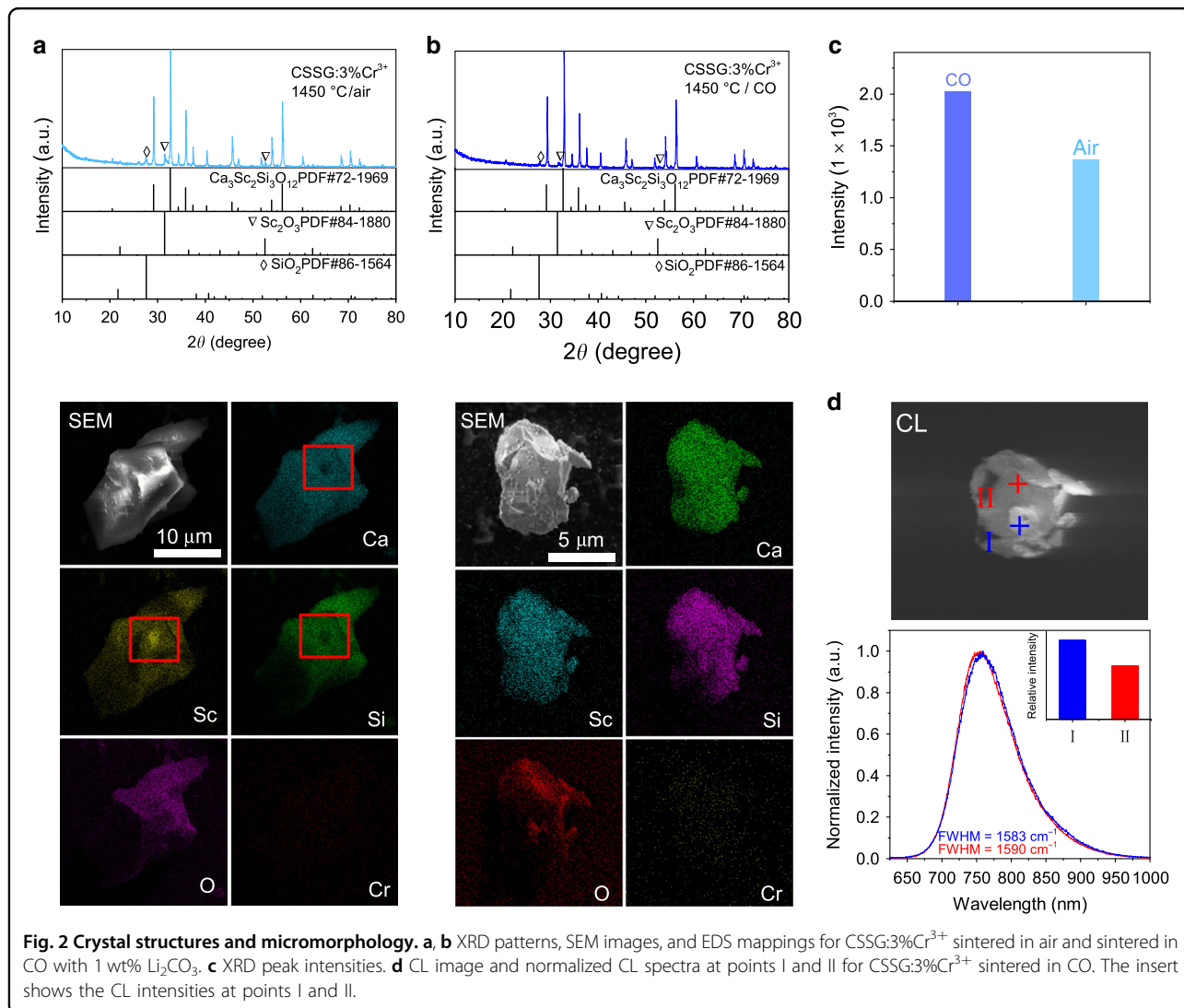
and electron paramagnetic resonance (EPR) results for CSSG:3% Cr^{3+} sintered in air and CO are given in Fig. 3. The binding energies at 99, 344, 399, and 528 eV are from Si-2p, Ca-2p, Sc-2p, and O-1s, respectively. The binding energy at 40 eV for Cr-3p is detected in the two samples⁴⁸. The changes in Cr are not apparent in the XPS spectra. However, in the DR spectra (Fig. 3c), the absorption band of Cr^{4+} (at ~1140 nm) is clearly identified for the sample sintered in air in addition to the absorption band of Cr^{3+} (at ~460 and 640 nm)^{34,35}. This means that some Cr^{3+} ions are oxidized into Cr^{4+} even though Cr_2O_3 is used as the raw material. For the sample sintered in CO, the Cr^{4+} absorption band almost disappears, and only the Cr^{3+} absorption band is observed. This means that Cr^{3+} is well maintained in the CO reducing atmosphere.

In the $3d^3$ electronic configuration of Cr^{3+} , three electrons occupy the d orbitals and give rise to a total spin of $S = 3/2$. ${}^4\text{A}_{2g}(\text{F})$ is the ground state for Cr^{3+} . In an octahedral crystal field, the ${}^4\text{F}$ state splits into a singlet orbital ${}^4\text{A}_{2g}$ and two orbitals ${}^4\text{T}_{1g}$ and ${}^4\text{T}_{2g}$, thus causing EPR signals⁴⁹. As Fig. 3d shows, the sharp peaks at $g = 3.8$ – 3.9 belong to the isolated Cr^{3+} ion, and the peaks at approximately $g = 2$ represent the first neighbor Cr^{3+} – Cr^{3+} pair^{42–44,49}. The EPR intensity for the sample sintered in CO is stronger than that for the sample sintered in air, demonstrating an increased ratio of Cr^{3+} . Combining the DR and EPR results, it is claimed that Cr^{3+} can be maintained and increased in the reducing atmosphere, which is another reason for the improvement of the Cr^{3+} NIR luminescence.

Temperature-dependent NIR emissions

Figure 4a–c shows the temperature-dependent luminescence of CSSG:6% Cr^{3+} . The integrated PL intensity at 25 °C is set as the normalized standard, and 97.4% can still be maintained at 150 °C for the phosphor sintered in CO, whereas 85.6% can be maintained for the phosphor sintered in air. The temperature dependence of the emission intensity can be well fitted by the Arrhenius formula, and the activation energy is calculated to be $\Delta E = 0.336$ eV for the optimized sample, compared with $\Delta E = 0.220$ eV for the initial sample (Fig. 4b). When the temperature increases from 25 to 300 °C, the peak position redshifts from ~783 to ~807 nm (Fig. 4d), attributed to the decreased CF caused by lattice expansion. The FWHM increases from 1483 to 1551 cm^{-1} (92.3 to 100.2 nm), attributed to the strengthened EPC effect that will be discussed in the following.

Figure 4e shows the PLE and PL spectra of CSSG:6% Cr^{3+} at 77 K with a step size of 0.05 nm. The transitions from ${}^4\text{A}_{2g}$ to ${}^4\text{T}_{2g}({}^4\text{F})$ and ${}^4\text{T}_{1g}({}^4\text{F})$ are centered at 15,670 cm^{-1} (~636 nm) and 22,050 cm^{-1} (~453 nm), respectively. The R-line is only detected in the PLE spectrum at 698.3 nm (~14,320 cm^{-1}). The peak at



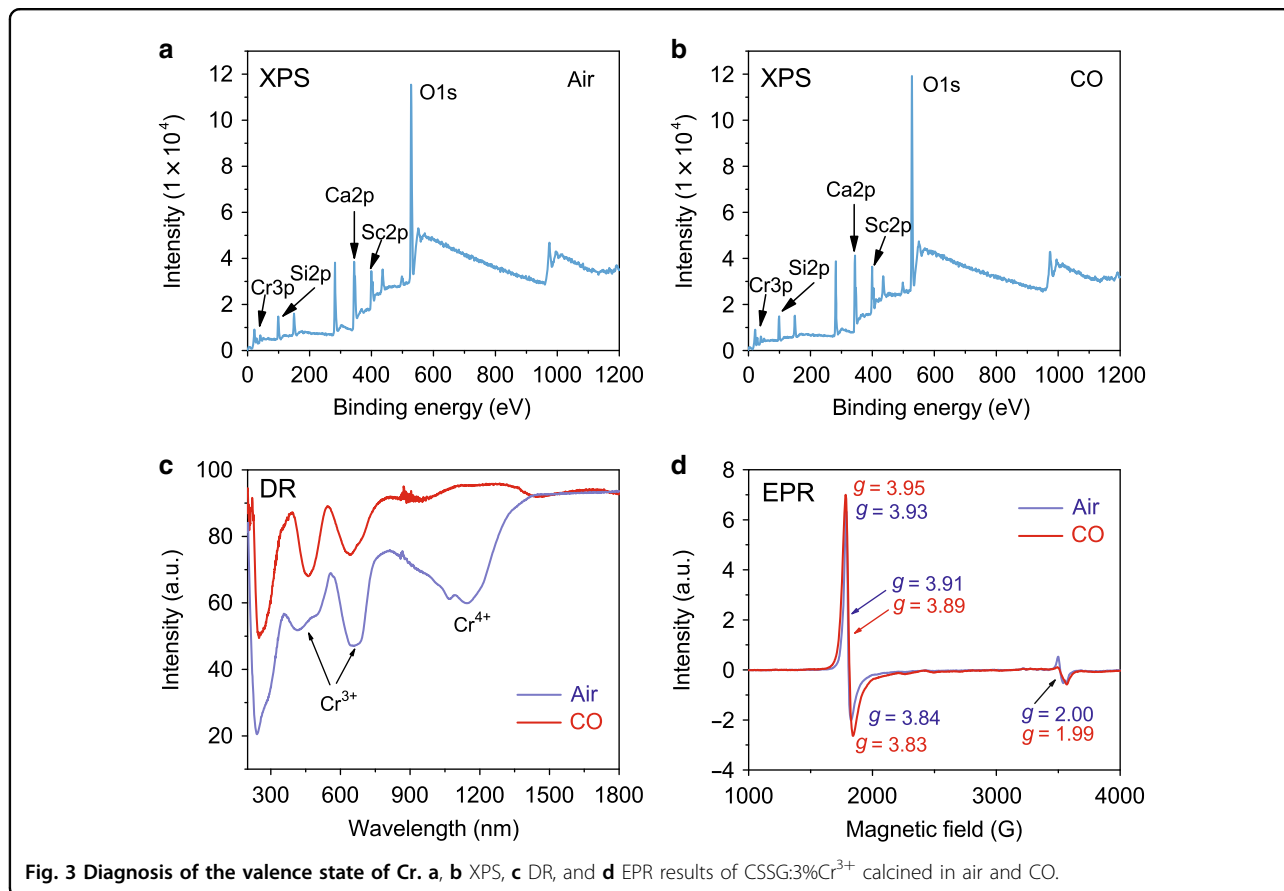
~ 713 nm ($\sim 14,030$ cm⁻¹) is observed in both the PL and PLE spectra, which is assigned to the zero-phonon line (ZPL) for the ${}^4T_{2g}({}^4F)$ and ${}^4A_{2g}$ transition (Fig. S7). The energy gap between ${}^2E_g({}^2G)$ and the ${}^4T_{2g}({}^4F)$ ZPL was evaluated to be ~ 290 cm⁻¹, indicating a strong spin-orbit coupling (SOC) of the ${}^2E_g({}^2G)$ and ${}^4T_{2g}({}^4F)$ states⁵⁰. Thus, the fluorescent decay curve shows a biexponential model with a lifetime of ~ 190 μ s (Fig. S8–S9).

The PL spectrum has a maximum peak at $\sim 12,980$ cm⁻¹ (~ 770 nm) with a FWHM of 1560 cm⁻¹ (~ 93 nm). The corresponding Stokes shift is ~ 2700 cm⁻¹. The peak at 730 nm ($\sim 13,700$ cm⁻¹) is the phonon satellite of the ZPL. The energy difference between the ZPL and its phonon satellite is determined to be ~ 330 cm⁻¹, which corresponds to one of the vibrational modes ($\hbar\omega$) that couple with the ${}^4T_{2g}({}^4F) \rightarrow {}^4A_{2g}$ transition (Fig. S7).

A Stokes shift has a relationship of $(2S + 1)\hbar\omega$, where S is the Huang–Rhys parameter; thus, S is determined

to be between 3 and 4, which is smaller than the value (~ 6) for LSGG:Cr³⁺³¹. Both the broadband emissive characteristic and the large Stokes shift indicate a stronger EPC for the ${}^4T_{2g}({}^4F) \rightarrow {}^4A_{2g}$ transition in CSSG:Cr³⁺. A stronger EPC leads to a larger S value^{28–31}. At a low temperature (77 K), the EPC effect is weak. Thus, the FWHM value at 77 K decreases by ~ 190 cm⁻¹ compared with the FWHM of 1750 cm⁻¹ (~ 110 nm) at RT.

It is worth noting that the ratio in the range of 650–725 nm increases and the emission shows a blueshift with increasing temperature. The small energy gap (~ 290 cm⁻¹) between 2E_g and the ${}^4T_{2g}$ ZPL leads to mixing of the ${}^2E_g({}^2G)$ and ${}^4T_{2g}({}^4F)$ states. When the temperature increases, electronic transfer from the ${}^4T_{2g}$ state to the 2E_g state is strengthened with the assistance of EPC. Thus, the radiative transitions from the ${}^2E_g({}^2G)$ state increase, and blueshifts are observed.



Performance of the fabricated NIR-LED device

The CSSG:6%Cr³⁺ phosphor shows a green color (Fig. 5a). Based on the optimized phosphor and a high-power blue chip, an NIR-LED device was fabricated and is displayed in Fig. 5b–d. The electroluminescence (EL) spectra, optical powers, and conversion efficiencies of the device depending on the driving current (I) are given in Fig. 5e–h. The strong emission peak at ~ 460 nm comes from the blue chip. The broad NIR emission band comes from CSSG:Cr³⁺. The optical powers of both the total radiance and NIR light increase with increasing current until reaching maxima of 97.8 and 64.7 mW, respectively, at 520 mA.

The conversion efficiency from the emitted blue light to NIR light ($\eta_{\text{NIR/blue light}}$) drops from 33.5 to 12.3% when the driving current increases from 100 to 600 mA. Correspondingly, the conversion efficiency from the input electronic power to NIR emissions ($\eta_{\text{NIR/input}}$) decreases from 7.2 to 2.3%. $\eta_{\text{NIR/input}}$ is much lower than $\eta_{\text{NIR/blue light}}$. The lower photoelectric conversion efficiency ($\eta_{\text{blue light/input}}$) from the input electronic power to blue light should be responsible for this phenomenon because the $\eta_{\text{blue light/input}}$ of the used blue chip, ranging from 31.9 to 19.4% at 100–600 mA, is not very high (Fig. S9). If the used blue chip is efficient, then $\eta_{\text{NIR/input}}$ can be greatly enhanced further.

On the other hand, only 84.3% of the NIR emission can be detected due to the limitation of the measurement range, up to 850 nm (Fig. 5h). If the 15.7% unmeasured part is taken into account, then the actual NIR optical power should be 76.8 mW at 520 mA. Thus, the total optical power even reaches 109.9 mW, which is much higher than the performances reported until now⁴⁴.

The QEs discussed above are the measured results. The QE and radiant power were measured by using the same spectrometer. If the unmeasured part is also taken into account, then the IQE and EQE can actually reach 92.3% and 25.5%, respectively, which are almost the best results as far as we know up to now.

Applications in night vision

Figure 6 shows the application of the NIR-LED for night vision. Visible images taken by a visible camera are colorful when water, milk, and cups are illuminated by either fluorescent light or NIR light. The logo is clear under fluorescent light. However, only black-and-white images are captured by an NIR camera. When the NIR-LED is off, nothing can be captured. When the NIR-LED is on, the logo is much clearer when it is taken by the NIR camera than when it is taken by the visible camera, especially the

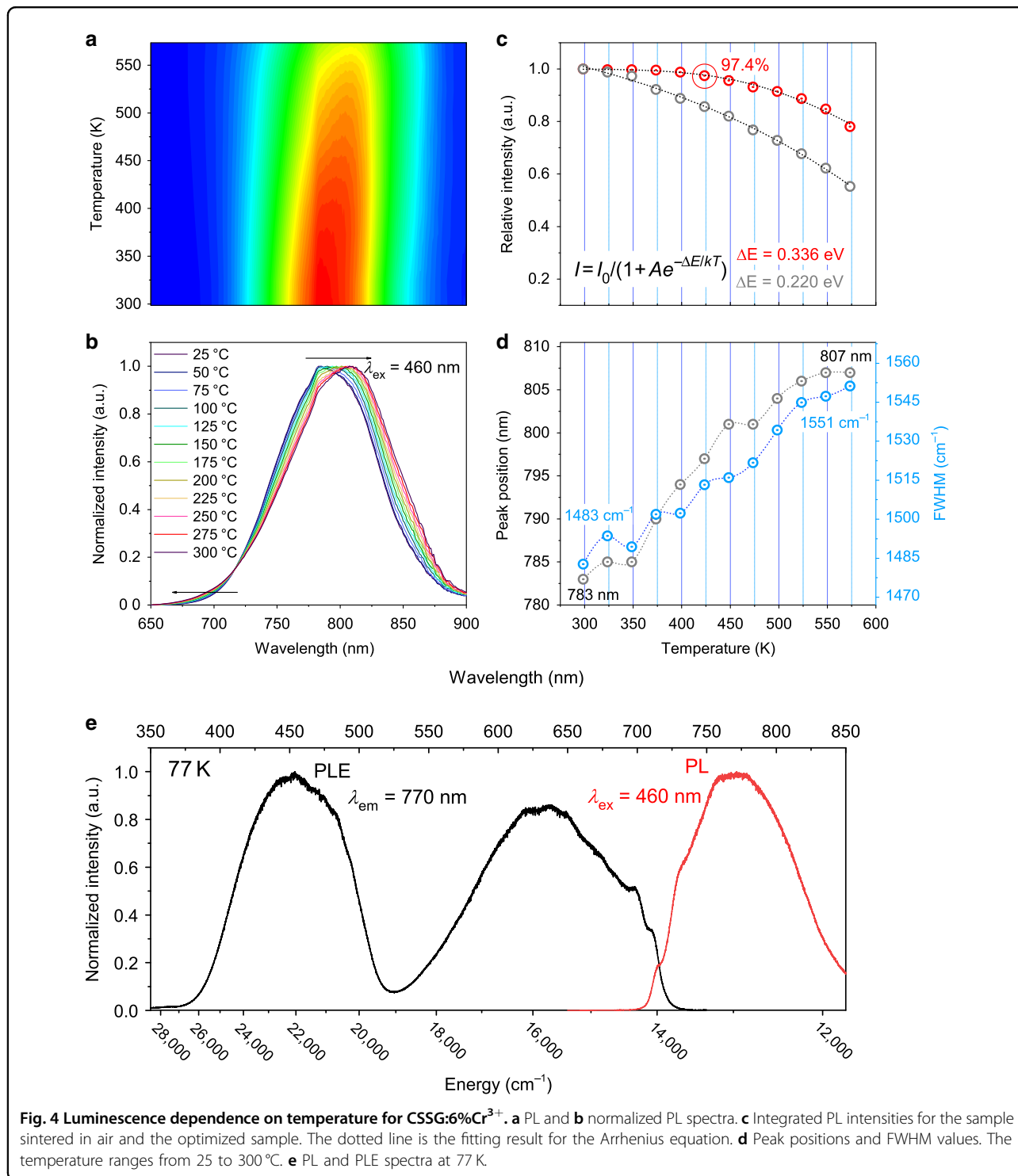
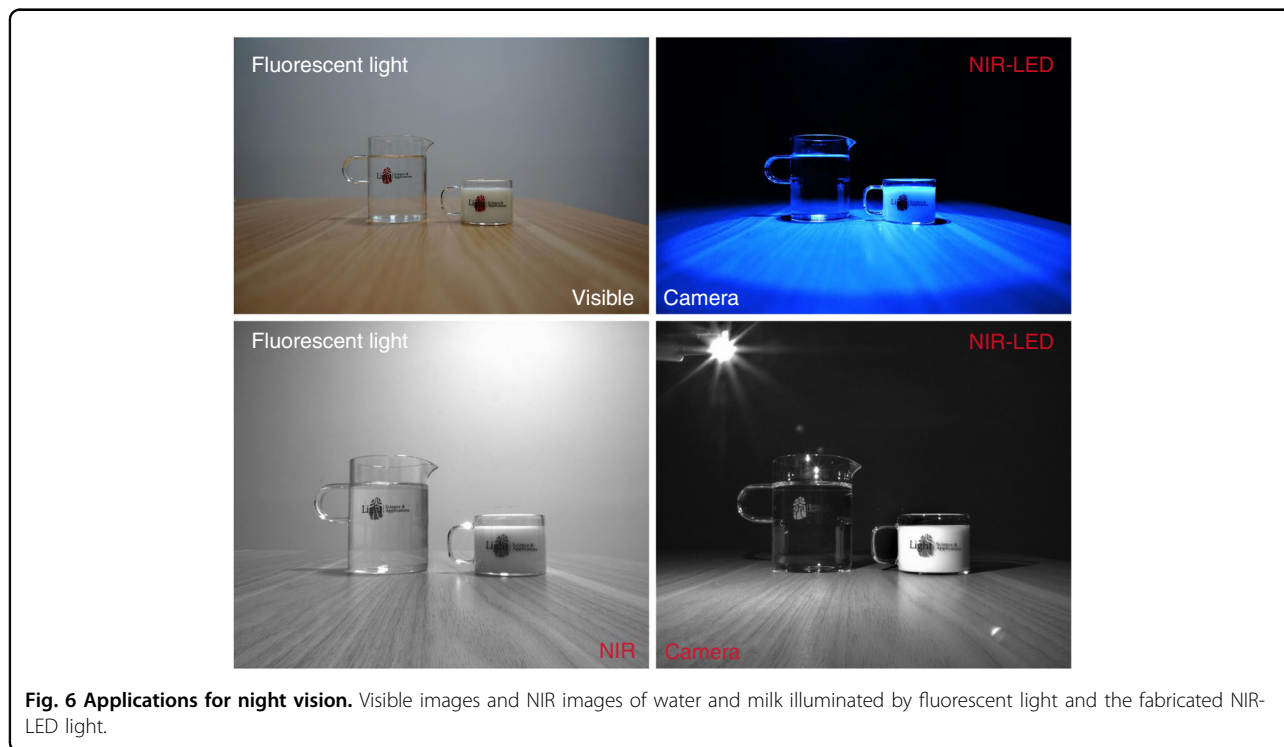
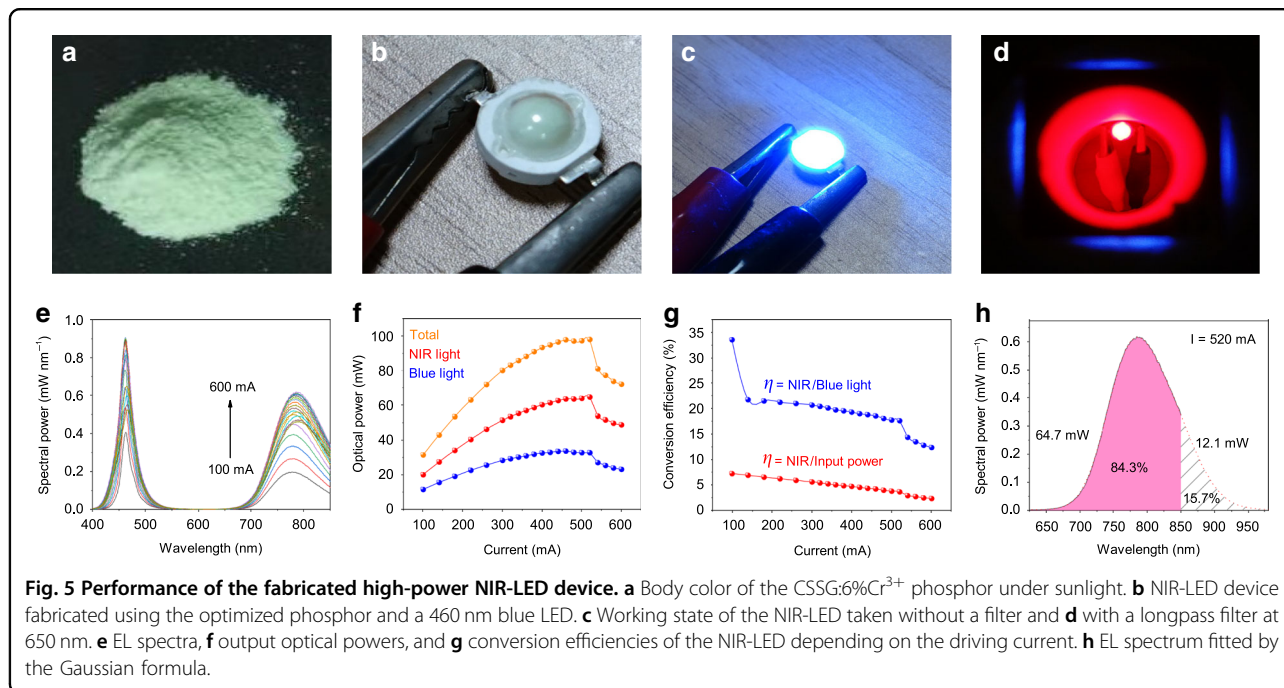


Fig. 4 Luminescence dependence on temperature for CSSG:6%Cr³⁺. **a** PL and **b** normalized PL spectra. **c** Integrated PL intensities for the sample sintered in air and the optimized sample. The dotted line is the fitting result for the Arrhenius equation. **d** Peak positions and FWHM values. The temperature ranges from 25 to 300 °C. **e** PL and PLE spectra at 77 K.

logo on the surface of the glass filled with transparent water. These results indicate that the achieved CSSG:Cr³⁺ phosphor enables the NIR-LED to have good application in night-vision technology. Potential applications in monitoring foods and medicines are also expected for such NIR phosphors and NIR-LED light sources.

Discussion

In conclusion, CSSG:Cr³⁺ exhibits broad NIR emission from 700 to 900 nm under blue light excitation. The previously reported CSSG:Cr³⁺ synthesized in air has low IQE (12.8%) and EQE (4.8%), limiting its performance in pc-NIR-LED devices. By adding fluxes and synthesizing in



a CO reducing atmosphere, the IQE and EQE are greatly improved to 77.8% and 21.5%, respectively. If the unmeasured part is taken into account, then the actual IQE and EQE should reach 92.3% and 25.5%, respectively, which is almost the best result among the NIR phosphors developed until now. Investigation of the crystal

structures and micromorphology demonstrated that the improvement arises from the modification of the crystallinity and the maintenance of Cr³⁺. The achieved CSSG:6%Cr³⁺ exhibits excellent thermal stability, and 97.4% of the emission intensity at room temperature can still be maintained at 150 °C. Thus, when it was used in a

high-power blue chip, the fabricated NIR-LED showed a high optical power of nearly 110 mW at 520 mA, which is almost the best performance among NIR-LED light sources.

Among the reported NIR phosphors, Cr^{3+} is an important activator, and its luminescence is determined by both the selected host and the synthesis technology. We believe that this work provides an effective strategy to optimize NIR phosphors using only a simple but the best method. Thus, it will inspire more researchers to achieve much better performance of known NIR phosphors and advance development of next-generation smart NIR-LED light sources.

Materials and methods

Synthesis

Samples with the nominal composition of $\text{Ca}_3\text{Sc}_{2-x}\text{Si}_3\text{O}_{12}:y\text{Cr}^{3+}$, $x\text{wt}\%$ flux were synthesized by a high-temperature solid-state reaction. The starting materials of CaCO_3 (99.9%), Sc_2O_3 (99.9%), SiO_2 (AR), and Cr_2O_3 (99.95%) and fluxes of NH_4F , CaF_2 , H_3BO_3 , LiF , and Li_2CO_3 were weighed according to the nominal composition and then ground in an agate mortar for 30 min. After that, the powders were sintered at 1450 °C for 3 h in air and a CO atmosphere.

Fabrication of pc-NIR-LEDs

NIR-LEDs were fabricated using the optimized NIR phosphor CSSG:6% Cr^{3+} and high-power blue-LED chips (460 nm). The phosphors were thoroughly mixed with epoxy resin and then coated on the chips.

Characterization

XRD patterns were measured by a Bruker D8 X-ray diffractometer with $\text{Cu K}\alpha$ radiation ($\lambda = 1.54056 \text{ \AA}$) at 40 kV and 40 mA. DR spectra were measured by a LAMBDA 950. PL and PLE spectra at RT–300 °C were characterized by a Hitachi F-4600. PL and PLE spectra at 77 K were measured by a Horiba FL-311 by dipping the sample in liquid nitrogen. EPR data were recorded on a Bruker E500 with the X-band frequencies ($\approx 9.845 \text{ GHz}$) and a microwave power of 0.63 mW. XPS was performed on a Kratos Axis Ultra DLD. IQEs and EQEs were recorded by an Otsuka Photonic Electronics QE-2100. A field-emission scanning electron microscope (FE-SEM, Hitachi S-4800) equipped with an energy dispersive X-ray spectroscopy (EDS) system and a CL system (MonoCL4, Gatan) was used to measure the morphology. EL spectra and performances of fabricated pc-NIR-LED devices were measured by an integrating sphere (Labsphere), and data were collected by a multichannel photodetector (MCPD-9800, Otsuka Photonic Electronics). Visible images and NIR images were taken by a visible camera (SONY

ILCE-7M2K) and an NIR camera (Work Power UC-500M), respectively.

Acknowledgements

This work is financially supported by the National Key Research and Development Program of China (2016YFC0104502, 2017YFC0111602), Fujian Institute of Innovation, Chinese Academy of Sciences (FJCXY18040203), Public Projects of Zhejiang Province (LGG18E020007), Science and Technology Major Project of Ningbo Municipality (2017C110028), and Natural Science Foundation of Shanxi Province (201801D121020, 201801D221132).

Author details

¹Ningbo Institute of Materials Technology & Engineering, Chinese Academy of Sciences, Ningbo 315201, China. ²College of Physics and Optoelectronics, Taiyuan University of Technology, Taiyuan 030024, China. ³University of Chinese Academy of Sciences, Beijing 100049, China. ⁴Department of Physics, Georgia Southern University, Stateboro, GA 30460, USA

Author contributions

Y.L. and L.W. initiated the research. The design of the experiments took shape with input from all the authors. Z.J. and C.Y. performed the experiments and measurement with support from P.S. and prepared the draft of the paper. X.W., H.J., and J.J. discussed the paper. All authors assisted in the editing of the final paper.

Conflict of interest

The authors declare that they have no conflict of interest.

Supplementary information is available for this paper at <https://doi.org/10.1038/s41377-020-0326-8>.

Received: 11 February 2020 Revised: 7 April 2020 Accepted: 28 April 2020
Published online: 15 May 2020

References

- Tang, X. et al. Dual-band infrared imaging using stacked colloidal quantum dot photodiodes. *Nat. Photonics* **13**, 277–282 (2019).
- Gu, Y. Y. et al. High-sensitivity imaging of time-domain near-infrared light transducer. *Nat. Photonics* **13**, 525–531 (2019).
- Tuong Ly, K. et al. Near-infrared organic light-emitting diodes with very high external quantum efficiency and radiance. *Nat. Photonics* **11**, 63–68 (2017).
- Pan, Z. W. et al. Sunlight-activated long-persistent luminescence in the near-infrared from Cr^{3+} -doped zinc gallogermanates. *Nat. Mater.* **11**, 58–63 (2011).
- Zeng, B. B. et al. Hybrid graphene metasurfaces for high-speed mid-infrared light modulation and single-pixel imaging. *Light: Sci. Appl.* **7**, 51 (2018).
- Liang, Y. J. et al. New function of the Yb^{3+} ion as an efficient emitter of persistent luminescence in the short-wave infrared. *Light: Sci. Appl.* **5**, e16124 (2016).
- Dincer, C. et al. Disposable sensors in diagnostics, food, and environmental monitoring. *Adv. Mater.* **31**, 1806739 (2019).
- Zampetti, A., Minotto, A. & Cacialli, F. Near-infrared (NIR) organic light-emitting diodes (OLEDs): challenges and opportunities. *Adv. Funct. Mater.* **29**, 1807623 (2019).
- Tessler, N. et al. Efficient near-infrared polymer nanocrystal light-emitting diodes. *Science* **295**, 1506–1508 (2002).
- Zhao, X. F. & Tan, Z. K. Large-area near-infrared perovskite light-emitting diodes. *Nat. Photonics* **14**, 215–218 (2020).
- Lukovic, M. et al. LED-based Vis-NIR spectrally tunable light source—the optimization algorithm. *J. Eur. Optical Soc.-Rapid Publ.* **12**, 19 (2016).
- Filippo, R., Taralli, E. & Rajteri, M. LEDs: sources and intrinsically bandwidth-limited detectors. *Sensors* **17**, 1673 (2017).
- Yao, Q. et al. YAG: Ce^{3+} transparent ceramic phosphors brighten the next-generation laser-driven lighting. *Adv. Mater.* <https://doi.org/10.1002/adma.201907888> (2020).
- Liu, Y. F. et al. An excellent cyan-emitting orthosilicate phosphor for NUV-pumped white LED application. *J. Mater. Chem. C* **5**, 12365–12377 (2017).

15. Liu, Y. F. et al. $\text{Ba}_9\text{Lu}_2\text{Si}_6\text{O}_{24}\text{Ce}^{3+}$: an efficient green phosphor with high thermal and radiation stability for solid-state lighting. *Adv. Optical Mater.* **3**, 1096–1101 (2015).
16. Wei, Y. et al. New strategy for designing orangish-red-emitting phosphor via oxygen-vacancy-induced electronic localization. *Light: Sci. Appl.* **8**, 15 (2019).
17. Zhao, M. et al. Emerging ultra-narrow-band cyan-emitting phosphor for white LEDs with enhanced color rendition. *Light: Sci. Appl.* **8**, 38 (2019).
18. Senden, T. et al. Quenching of the red Mn^{4+} luminescence in Mn^{4+} -doped fluoride LED phosphors. *Light: Sci. Appl.* **7**, 8 (2018).
19. Dai, P. P. et al. A single Eu^{2+} -activated high-color-rendering oxychloride white-light phosphor for white-light-emitting diodes. *Light: Sci. Appl.* **5**, e16024 (2016).
20. De Guzman, G. N. A. et al. Near-infrared phosphors and their full potential: a review on practical applications and future perspectives. *J. Lumin.* **219**, 116944 (2020).
21. Du, J. R. & Poelman, D. Identifying near-infrared persistent luminescence in Cr^{3+} -doped magnesium gallogermanates featuring afterglow emission at extremely low temperature. *Adv. Optical Mater.* **8**, 1901848 (2020).
22. Lyu, T. S. & Dorenbos, P. Designing thermally stimulated $1.06\ \mu\text{m}$ Nd^{2+} emission for the second bio-imaging window demonstrated by energy transfer from Bi^{3+} in La -, Gd -, Y -, and LuPO_4 . *Chem. Eng. J.* **372**, 978–991 (2019).
23. Song, E. H. et al. Heavy Mn^{2+} doped MgAl_2O_4 phosphor for high-efficient near-infrared light-emitting diode and the night-vision application. *Adv. Optical Mater.* **7**, 1901105 (2019).
24. Qiao, J. W. et al. Divalent europium-doped near-infrared-emitting phosphor for light-emitting diodes. *Nat. Commun.* **10**, 5267 (2019).
25. Zhao, F. Y. et al. Double perovskite $\text{Cs}_2\text{AgInCl}_6\text{Cr}^{3+}$: broadband and near-infrared luminescent materials. *Inorg. Chem. Front.* **6**, 3621–3628 (2019).
26. Wang, C. P. et al. An ultra-broadband near-infrared Cr^{3+} -activated gallogermanate $\text{Mg}_3\text{Ga}_2\text{GeO}_8$ phosphor as light sources for food analysis. *ACS Appl. Electron. Mater.* **1**, 1046–1053 (2019).
27. Dai, D. J. et al. Broad band emission near-infrared material $\text{Mg}_3\text{Ga}_2\text{GeO}_8\text{Cr}^{3+}$: substitution of Ga - In , structural modification, luminescence property and application for high efficiency LED. *J. Alloy. Compd.* **806**, 926–938 (2019).
28. Malysa, B., Meijerink, A. & Jüstel, T. Temperature dependent luminescence Cr^{3+} -doped $\text{GdAl}_3(\text{BO}_3)_4$ and $\text{YAl}_3(\text{BO}_3)_4$. *J. Lumin.* **171**, 246–253 (2016).
29. Malysa, B. et al. On the influence of calcium substitution to the optical properties of Cr^{3+} doped SrSc_2O_4 . *J. Lumin.* **190**, 234–241 (2017).
30. Malysa, B., Meijerink, A. & Jüstel, T. Temperature dependent photoluminescence of Cr^{3+} doped $\text{Sr}_8\text{MgLa}(\text{PO}_4)_7$. *Optical Mater.* **85**, 341–348 (2018).
31. Malysa, B., Meijerink, A. & Jüstel, T. Temperature dependent Cr^{3+} photoluminescence in garnets of the type $\text{X}_3\text{Sc}_2\text{Ga}_3\text{O}_{12}$ ($\text{X}=\text{Lu}, \text{Y}, \text{Gd}, \text{La}$). *J. Lumin.* **202**, 523–531 (2018).
32. Zeng, H. T. et al. Two-site occupation for exploring ultra-broadband near-infrared phosphor - double-perovskite $\text{La}_2\text{MgZrO}_6\text{Cr}^{3+}$. *Chem. Mater.* **31**, 5245–5253 (2019).
33. Yu, D. C. et al. Non-rare-earth $\text{Na}_3\text{AlF}_6\text{Cr}^{3+}$ phosphors for far-red light-emitting diodes. *ACS Appl. Electron. Mater.* **1**, 2325–2333 (2019).
34. Zhang, L. L. et al. Cr^{3+} -doped broadband NIR garnet phosphor with enhanced luminescence and its application in NIR spectroscopy. *Adv. Optical Mater.* **7**, 1900185 (2019).
35. Zhang, L. L. et al. A high efficiency broad-band near-infrared $\text{Ca}_2\text{LuZr}_2\text{Al}_3\text{O}_{12}$: Cr^{3+} garnet phosphor for blue LED chips. *J. Mater. Chem. C* **6**, 4967–4976 (2018).
36. Shao, Q. Y. et al. Photoluminescence properties of a $\text{ScBO}_3\text{Cr}^{3+}$ phosphor and its applications for broadband near-infrared LEDs. *RSC Adv.* **8**, 12035–12042 (2018).
37. Xu, X. X. et al. Highly efficient and thermally stable Cr^{3+} -activated silicate phosphors for broadband near-infrared LED applications. *Chem. Eng. J.* **383**, 123108 (2020).
38. Shao, Q. Y. et al. Broadband near-infrared light source derived from Cr^{3+} -doped phosphors and a blue LED chip. *Opt. Lett.* **43**, 5251–5254 (2018).
39. Yao, L. Q. et al. Broadband emission of single-phase $\text{Ca}_3\text{Sc}_2\text{Si}_3\text{O}_{12}\text{Cr}^{3+}/\text{Ln}^{3+}$ ($\text{Ln} = \text{Nd}, \text{Yb}, \text{Ce}$) phosphors for novel solid-state light sources with visible to near-infrared light output. *Ceram. Int.* **45**, 14249–14255 (2019).
40. Hayashi, D. et al. A broadband LED source in visible to short-wave-infrared wavelengths for spectral tumor diagnostics. *Appl. Phys. Lett.* **110**, 233701 (2017).
41. Huang, W. T. et al. Broadband Cr^{3+} , Sn^{4+} -doped oxide nanophosphors for infrared mini light-emitting diodes. *Angew. Chem. Int. Ed.* **58**, 2069–2072 (2019).
42. Lee, C. et al. Chromium(III)-doped fluoride phosphors with broadband infrared emission for light-emitting diodes. *Inorg. Chem.* **59**, 376–385 (2020).
43. Rajendran, V. et al. Super broadband near-infrared phosphors with high radiant flux as future light sources for spectroscopy applications. *ACS Energy Lett.* **3**, 2679–2684 (2018).
44. Rajendran, V. et al. Ultra-broadband phosphors converted near-infrared light emitting diode with efficient radiant power for spectroscopy applications. *ACS Photonics* **6**, 3215–3224 (2019).
45. Shimomura, Y. et al. Photoluminescence and crystal structure of green-emitting $\text{Ca}_3\text{Sc}_2\text{Si}_3\text{O}_{12}\text{Ce}^{3+}$ phosphor for white light emitting diodes. *J. Electrochem. Soc.* **154**, J35–J38 (2007).
46. Liu, Y. F. et al. Generation of broadband emission by incorporating N^{3-} into $\text{Ca}_3\text{Sc}_2\text{Si}_3\text{O}_{12}\text{Ce}^{3+}$ garnet for high rendering white LEDs. *J. Mater. Chem.* **21**, 6354–6358 (2011).
47. Liu, Y. F. et al. Tunable full-color-emitting $\text{Ca}_3\text{Sc}_2\text{Si}_3\text{O}_{12}\text{Ce}^{3+}$, Mn^{2+} phosphor via charge compensation and energy transfer. *Chem. Commun.* **47**, 10677–10679 (2011).
48. Scierka, S. J. et al. Determination of the distribution of chromium oxidation states in reduced $\text{Cr}/\text{Al}_2\text{O}_3$ catalysts from XPS by factor analysis and curve fitting. *Surf. Interface Anal.* **20**, 901–908 (1993).
49. Edgar, A. & Hutton, D. R. Exchange-coupled pairs of Cr^{3+} ions in emerald. *J. Phys. C: Solid State Phys.* **11**, 5051–5063 (1978).
50. Struve, B. & Huber, G. The effect of the crystal field strength on the optical spectra of Cr^{3+} in gallium garnet laser crystals. *Appl. Phys. B* **36**, 195–201 (1985).